Metal oxide decorated carbon nanocomposite electrodes for propofol monitoring

David C. Ferrier [*], Janice Kiely , Richard Luxton

Institute of Bio-Sensing Technology, University of the West of England, Frenchay Campus, Bristol, BS16 1QY, United Kingdom

ARTICLE INFO

ABSTRACT

Despite the growing evidence of the benefits of total-intravenous anaesthesia using propofol compared to conventional volatile-based anaesthesia, both in terms of environmental impact and patient outcomes, the majority of administered general anaesthetics use volatile agents. A significant reason for this is the lack of suitable methods for continuous, real-time propofol monitoring. Here we present a cytochrome P450 2B6/carbon nanotube/graphene oxide/metal oxide nanocomposite sensor for propofol monitoring. The enzyme prevents electrode fouling by converting the propofol into a quinone/quinol redox pair and the nanocomposite enables rapid and sensitive detection. The nanocomposite was synthesised via a simple 'green synthesis'-based approach using an extract of common bay laurel. It was found that composites containing iron oxide nanoparticles resulted in the best performance, with a limit of detection of 7.0 ± 0.7 ng/ml and a sensitivity of 29.9 ± 6.4 nA/μg/ml/ mm^2. The sensor demonstrated good specificity with respect to several common perioperative drugs, propofol detection was demonstrated in a 'serum-like' solution and produced a linear response across the therapeutic range of propofol (1–10 μg/ml).

1. Introduction

Propofol (2,6-diisopropylphenol) is one of the most commonly used intravenous anaesthetics (Kivlehan et al., 2015; Sahinovic et al., 2018). There is a growing body of evidence that total intravenous anaesthesia (TIVA) – wherein anaesthesia is both induced and maintained using intravenous drugs such as propofol – has many advantages over the more widely used volatile-based anaesthesia. These advantages include reduced cognitive effects (Lewis et al., 2007; Mellon et al., 2007; Xie et al., 2007), the potential of improved survival rates for cancer patients (Wigmore et al., 2016; Wall et al., 2019) and a significantly reduced environmental impact (Ryan and Nielsen, 2010; Campbell and Pierce, 2015; Vollmer et al., 2015). Despite these advantages, TIVA only accounts for a minority of general anaesthetics performed worldwide (Laurila et al., 2011). A major reason for this is a lack of suitable techniques for continuous, real-time monitoring of patient blood propofol concentrations (Ferrier et al., 2022). Current methods for determining propofol infusion rates involve mathematical models based on pharmacokinetic data. However, these models are often unreliable (Laurila et al., 2011; Zhang et al., 2017). In addition to surgical applications, propofol is one of the most common drugs used for sedation in intensive

care units (ICUs) (Barr et al., 2001, 2013; Yamamoto, 2020). In this context there is the added complexity that propofol kinetics can vary considerably in ICU patients (Barr et al., 2001), rendering models even less reliable. The issue of sedation monitoring in ICU patients has risen in prominence recently as a result of the global surge of patients undergoing mechanical ventilation in ICUs as a result of the COVID-19 pandemic.

Propofol can be detected electrochemically, but its oxidation produces non-conductive polymers leading to rapid electrode passivation (Ferreira et al., 2006; Yang et al., 2013). In a previous publication (Ferrier et al., 2021) we introduced an electrochemical sensor based on the enzyme cytochrome P450 2B6. The enzyme converts propofol to a quinone/quinol redox couple which can be easily detected electrochemically, thereby circumventing the electrode passivation problem. This sensor demonstrated a limit of detection below the lower end of the therapeutic range for propofol. However, greater sensitivity will be required for real-world applications as it is known that as little as 2% of propofol in serum exists free in solution, with the rest being bound to erythrocytes or serum proteins (Mazoit and Samii, 1999).

Metal oxide nanoparticles are widely used in electrochemical sensors to increase electrode surface area, improve electron transfer, and for

their catalytic properties (Lim and Gao, 2015). Common examples are zinc oxide (Tak et al., 2013; Wayu et al., 2013; Hwa and Subramani, 2014), copper oxide (Chen et al., 2016; Mdletshe et al., 2019) and iron oxide (Aryal and Jeong, 2019; Tung et al., 2019) which are chosen for their favourable electrical characteristics, high stability and low cost. In recent years, 'green synthesis' – whereby metal nanoparticles are synthesised via biological routes such as bacteria, fungi and plant extracts – has emerged as an exciting area of research, allowing for simple nanoparticle synthesis without relying on expensive or environmentally damaging materials or processes (Makarov et al., 2014; Zikalala et al., 2018).

Graphene is frequently used in biosensor applications as it possesses very favourable properties, including very high surface area to volume ratio, high electrical conductivity and high stability (Madhurantakam et al., 2017; Rostamabadi and Heydari-Bafrooei, 2019). Graphene oxide is also commonly used, for whilst its electrical conductivity is lower than for pure graphene, it has greater biocompatibility and is more readily chemically functionalised (Zhao et al., 2019). Carbon nanotubes (CNTs) are often used in conjunction with graphene or graphene oxide because, in addition to also having excellent electrical characteristics and high surface area to volume ratios, they can act as spacers to prevent agglomeration or stacking of graphene (Asadian et al., 2017).

Herein we present a metal oxide-decorated graphene oxide/carbon nanotube/cytochrome P450 2B6 functionalised electrochemical sensor for the detection of propofol. The decoration of the graphene oxide with metal oxide nanoparticles is undertaken using an extract from *laurus nobilis* (bay laurel). The decorated graphene oxide is mixed with multi-walled carbon nanotubes (MWCNTs) to produce a nanocomposite which is drop-cast onto a screen-printed electrode. The enzyme cytochrome P450 2B6 is expressed within deactivated yeast cells, which are in turn immobilised alongside gold nanoparticles within a chitosan film deposited on top of the nanocomposite layer. In the presence of the cofactor NADPH, the enzyme will convert propofol into a quinone/quinol redox couple which can be detected using simple electrochemistry. The best of the authors' knowledge, this work represents the first application of carbon/metal oxide nanocomposites to propofol detection and represents one of the very few applications of the green synthesis of nanoparticles to sensor development.

2. Materials and methods

2.1. Materials

Dried bay laurel leaves were purchased from JustIngredients Ltd. (UK). These were thoroughly rinsed with deionised water and dried prior to use. All other materials were purchased from Merck (Dorset, UK) and used as supplied.

The graphene oxide (GO) is 4–10% edge oxidised, and the multi-walled carbon nanotubes (MWCNTs) are carboxylic acid functionalised (>8%) with average dimeter 9.5 nm and length 1.5 μm.

Copper (II) chloride ($CuCl_2$, 97%) and iron (III) chloride ($FeCl_3$, 97%) were dissolved in deionised water to produce 0.1 M solutions.

2,6-diisopropylphenol (97%) was diluted in dimethyl sulfoxide (DMSO, 99.9%) to produce a 10 mM solution. This solution was further diluted with 10 mM phosphate buffered saline (PBS, 2.7 mM KCl, 137 mM NaCl, pH 7.4) to produce a 1 mM solution.

Lidocaine and cisatracurium besilate were dissolved in DMSO to produce 10 mM solutions. These solutions were then diluted to either 1 mM (lidocaine) or 100 μM (cisatracurium besilate) with 10 mM PBS.

1 mg/ml solutions in methanol of morphine, fentanyl and midazolam were diluted with 10 mM PBS to produce 10 μM solutions.

The testing medium was prepared by dissolving β-nicotinamide adenine dinucleotide phosphate sodium salt ($NADP^+$) and D-glucose-6-phosphate dipotassium salt hydrate (G6P) to a concentration of 50 μg/ml in 10 mM PBS.

A potassium ferricyanide solution was prepared by dissolving $K_3[Fe(CN)_6]$ and KNO_3 in deionised water at concentrations of 0.1 and 1 M respectively.

2.2. Apparatus

All electrochemical measurements were performed using a PalmSens EmStat^3 potentiostat. The screen-printed electrodes (SPEs) were purchased from BVT Technologies (Strážek, Czech Republic) and consist of graphite working and counter electrodes and a silver/silver chloride (Ag/AgCl) pseudo-reference electrode. The working electrode diameter is 1 mm.

2.3. Nanocomposite synthesis

The metal oxide nanoparticles were synthesised using methods adapted from Jamzad et al. (Fakhari et al., 2019; Jamzad and Bidkorpeh, 2020). Bay leaf extract was prepared by grinding 20 g of dried bay leaves to a powder using a mortar and pestle. The powdered bay leaves were then added to 200 ml of deionised water and stirred at 80 °C for 10 min. The resultant solution was strained and then centrifuged to remove any remaining plant material. This bay leaf extract solution was stored at 4 °C until required and used within four weeks.

GO was added to 0.1 M metal salt solution (either $FeCl_3$ or $CuCl_2$) at a concentration of 1 mg/ml and sonicated for 30 min to ensure full dispersal. This mixture was added to bay leaf extract solution at a volume ratio of 1:1 and left at room temperature overnight to allow metal oxide nanoparticles to form.

The metal oxide nanoparticle-decorated graphene oxide was then extracted from solution by centrifuging at 5000 rpm for 15 min and washed by re-suspending in deionised water and re-centrifuging three times. The metal oxide nanoparticle-decorated graphene oxide was then suspended in deionised water at a GO concentration of 0.05 mg/ml, MWCNTs were added at a concentration of 0.1 mg/ml and the resultant mixture sonicated for 1 h to ensure full dispersion.

An equivalent concentration dispersion of MWCNT/GO was also prepared without functionalisation with metal oxide nanoparticles. Solutions of metal oxide nanoparticles without GO or MWCNTs were also prepared by mixing the metal salt solutions with the bay leaf extract solution as described above, for the purposes of characterisation of the resultant nanoparticles.

2.4. Nanoparticle characterisation

2.4.1. UV–vis spectroscopy

For the UV–vis analysis the metal oxide nanoparticle suspensions were sonicated for 10 min to ensure full dispersion. UV–vis absorption spectra were recorded over the range 220–750 nm using a DeNovix DS-11 Fx + spectrophotometer with a 10 mm path length.

2.4.2. Electron microscopy

5 μl samples of nanomaterial suspended in deionised water were deposited on carbon/pioloform film coated electron microscopy grids and left for 1 min to incubate before the excess was blotted away. The grids were then imaged using a FEI Tecnai12 BioTWIN transmission electron microscope fitted with a Ceta camera.

2.5. Electrode preparation

0.75 μl of the CNT/GO/metal oxide nanoparticle (MONP) dispersions described in Section 2.3 was drop-cast onto the working electrode of the SPEs and allowed to dry before a second 0.75 μl was drop-cast and dried in the same manner. The electrodes were then rinsed with deionised water to remove any unbound nanomaterial.

Preparation of the enzyme film has been described in a previous publication (Ferrier et al., 2021). Briefly, CypExpress 2B6 was suspended in phosphate buffer (pH7) at a concentration of 25 mg/ml and

this suspension mixed with a gold nanoparticle solution (approximately 0.25 mg/ml) and a 1% chitosan solution (1% acetic acid) in a ratio of 1:1:2 by volume. 1 μl of this mixture was deposited on top of the nanocomposite and left to dry at 4 °C. Once dry, the electrodes were immersed in 10 mM PBS for 30 min and then dried in air at room temperature. The functionalised electrodes were stored at 4 °C until use.

2.6. Electrochemical measurement

Differential pulse voltammetry measurements were performed on the CNT/GO/MONP/enzyme functionalised electrodes by depositing 50 μl of 10 μg/ml propofol solution (50 μg/ml NADP$^+$/G6P, 10 mM PBS) and performing sweeps between +0.2 and + 0.7 V, with a pulse of 50 mV, a step size of 20 mV, a pulse duration of 0.2 s and a scan rate of 50 mV/s. Prior to measurement, cyclic voltammetry was performed in 10 mM PBS solution between −0.8 and + 1.0 V at a scan rate of 50 mV/s until a stable baseline was achieved.

Amperometry measurements were performed on the enzyme functionalised electrodes by immersing them in 20 ml of 50 μg/ml NADP$^+$ and G6P solution (10 mM PBS) under stirring at room temperature. Aliquots of 1 mM propofol solution were injected at regular intervals. The sample interval was 0.5 s, and the working potential was +500 mV. Identical experiments were also performed using NADP$^+$/G6P solutions containing 5 wt% of bovine serum albumin (BSA) (heat shock fraction, pH 7, ≥98%).

Similar experiments were also performed injecting aliquots of lidocaine, cisatracurium besilate, morphine, fentanyl or midazolam solutions at regular intervals.

3. Results and discussion

3.1. Nanocomposite characterisation

3.1.1. UV–vis spectroscopy

The UV–vis absorption spectrum for the iron oxide nanoparticles is shown in Fig. 1a. It can be seen that there is a clear peak at

approximately 300 nm. The band-gap energy of the nanoparticles can be determined from the UV–vis data by the Tauc method (Viezbicke et al., 2015; Lassoued et al., 2018). The optical absorption strength is given by:

$$(\alpha h\nu)^{1/n} = A\left(h\nu - E_g\right) \qquad (1)$$

Where: α is the absorption coefficient, h is Plank's constant, ν is the optical frequency, A is a constant of proportionality and E_g is the band-gap energy. The value of n denotes the manner of the electron transition. Fig. 1b shows $(\alpha h\nu)^2$ versus hν (for a direct band-gap, $n = 1/2$). In the Tauc method, E_g is determined by the intercept of the extrapolation of the linear absorption edge (depicted by the dashed line) with the x-axis. In this manner it is determined that the direct band-gap energy of the iron oxide nanoparticles is approximately 3.5 eV. This value is higher than many other reported examples for both magnetite (Fe$_3$O$_4$) nanoparticles (El Ghandoor et al., 2012; Radoń et al., 2017; Bagbi et al., 2017) and hematite (α-Fe$_2$O$_3$) nanoparticles (Shi et al., 2007; Cesar et al., 2009; Gilbert et al., 2009; Alagiri and Hamid, 2014; Kamali et al., 2014), typically in the range 2–3 eV, but this can be accounted for by quantum size effects which can greatly influence the optical properties of nanomaterials (Thielsch et al., 1998). A potential mechanism for the formation of Fe$_3$O$_4$ nanoparticles by flavonoids and phenolic acids present in plant extracts has been proposed by Kobylinska et al. (2021).

Fig. 1c shows the UV–vis absorption spectrum for the copper oxide nanoparticles. It can be seen that there is a strong absorption peak at approximately 295 nm. Fig. 1d shows the corresponding Tauc plot for the direct band-gap from which it is determined that the direct band-gap energy is approximately 3.6 eV. Once again, this is higher than several other reported values for both cupric oxide (CuO) and cuprous oxide (Cu$_2$O), typically in the range 1–3 eV (Srivastava et al., 2013; Ghidan et al., 2016; Kumar et al., 2020), which can be accounted for by quantum size effects.

Tauc plots for the indirect band gaps ($n = 2$) for both the iron oxide and copper oxide nanoparticles are shown in the Supplementary Information, Figs. S1 and S2 respectively.
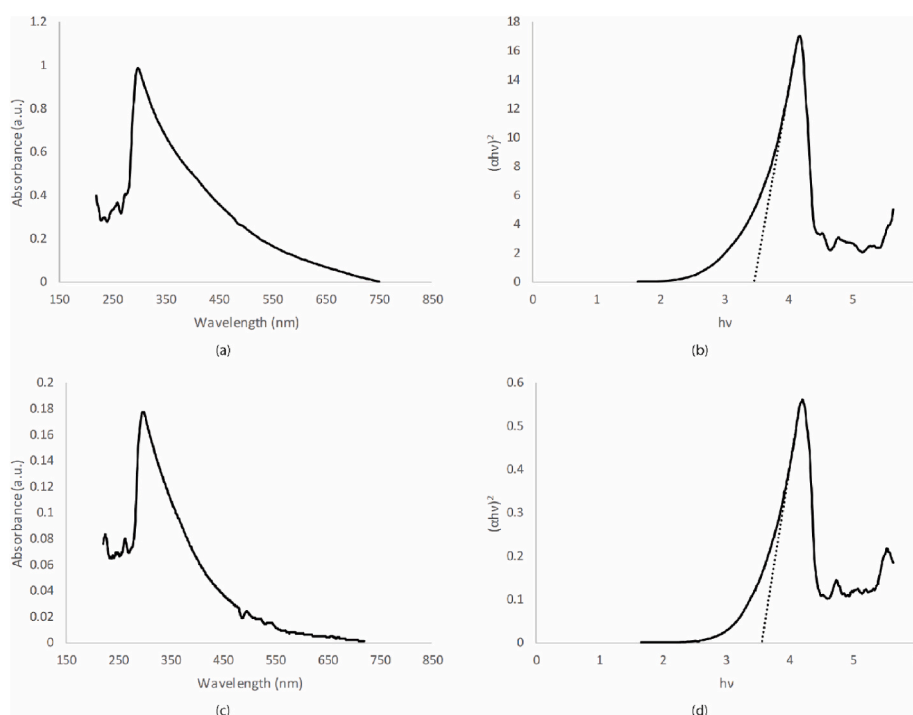
Fig. 1. a) UV–vis absorbance spectrum for iron oxide nanoparticles, b) Corresponding Tauc plot for direct band-gap (n = ½), c) UV–vis absorbance spectrum for copper oxide nanoparticles, d) Corresponding Tauc plot for direct band-gap.

3.1.2. Electron microscopy

The successful synthesis of metal oxide nanoparticles is confirmed by transmission electron microscopy (Fig. 2). Iron oxide and copper oxide nanoparticles are shown in Fig. 2a and b respectively, from which it can be seen that the resultant nanoparticles are roughly ellipsoidal in shape and have sizes ranging between approximately 10 and 100 nm, although they tend to form larger agglomerates.

3.2. Voltammetry measurements

Cyclic voltammograms for a blank SPE (i) and SPEs functionalised with CNT/GO (iii), CNT/GO/copper oxide nanoparticle (CuONP) (iv) and CNT/GO/iron oxide nanoparticle (FeONP) (ii) nanocomposites in potassium ferricyanide solution are shown in Fig. 3a. The ferricyanide reduction and oxidation peaks are both much closer together and much larger for the nanocomposite functionalised electrodes than for the blank electrode, indicating greater and more efficient electron transfer. This is as would be expected given the high surface area and favourable electrical characteristics of the nanomaterials. There is little difference in peak size and location between the CNT/GO nanocomposite functionalised electrodes and those functionalised with the MONP-decorated GO/CNT nanocomposites, indicating that the presence of the copper and iron oxide NPs do not impart improvements in terms of surface area or electron transfer.

Differential pulse voltammetry for electrodes functionalised with the different nanocomposites and the enzyme/chitosan film in the presence of propofol show a clear peak at approximately 380 mV (Fig. 3b) which corresponds to the oxidation of the product of the enzyme reaction, 2,6-diisopropylquinol. The position of the peak does not vary significantly for the different nanocomposites; however, the background current appears to vary significantly. The CNT/GO electrode displays the lowest background current, followed by the CNT/GO/FeONP electrode, with the CNT/GO/CuONP electrode displaying the highest background current.

3.3. Amperometry measurements

In order to counteract the effects of drift and noise that are common for sensors of this type, some simple signal processing was applied. Firstly, baseline correction was applied by performing a linear fit to the current response from the 5 min prior to the first injection of propofol solution and correcting all the data so that it is measured relative to this baseline. Secondly, smoothing was performed by applying a moving average filter to the current data with a bin size of 10 s. The bin size was decided upon as being a reasonable compromise between degree of smoothing and induced time-lag. An example of this is shown in the Supplementary Information, Fig. S3.

Fig. 4a shows the results of amperometry measurements for electrodes functionalised with CNT/GO (i), CNT/GO/CuO NP (ii), and CNT/GO/FeO NP (iii) for an increasing propofol concentration (aliquots of propofol stock solution are injected every 5 min). The average plateau current versus the resultant propofol concentration is shown in Fig. 4b.

It can be seen that all three sensors produce clear increases in current with increasing propofol concentration. These responses are fast, occurring within 1 min, and stable throughout the experiment. In all cases the current response is linear with respect to propofol concentration over the range investigated. As we have previously shown to be the case with sensors prepared in a similar manner without the addition of the nanocomposite (Ferrier et al., 2021), these sensors display no signs of electrode passivation as a result of the action of the cytochrome P450 2B6 enzyme, which converts the propofol into a quinone/quinol redox couple, thereby circumventing the fouling issue.

The sensitivity of the electrodes prepared using metal oxide decorated graphene oxide appears much greater than that of the sensor prepared using non-decorated graphene oxide. As discussed previously, the cyclic voltammetry results (Fig. 3a) do not suggest that improvements in terms of surface area or electron transfer are achieved through the inclusion of the metal oxide nanoparticles, suggesting that the improvements in sensitivity are the result of catalytic properties of the metal oxide nanoparticles. The concentration range shown in Fig. 4 represents only a small fraction of propofol's therapeutic range. However, as described previously, the majority of propofol will be protein bound, making this a more appropriate range over which to assess the sensor's performance in buffer solutions.

Table 1 shows the average sensitivities and limits of detection (LoD) for three replicates of CNT/GO, CNT/GO/CuONP and CNT/GO/FeONP electrodes (one example of each of which are shown in Fig. 4). The detection limit was determined using the calculation: $LoD = 3.3(\sigma_{low}/gradient)$, where σ_{low} is the standard deviation at a low propofol concentration. As already discussed, electrodes prepared using metal oxide decorated nanocomposites show significantly increased sensitivity compared to electrodes prepared using non-decorated nanocomposites, with FeO nanoparticles resulting in the greatest improvement. However, the LoD of the CNT/GO/CuONP electrodes is higher than that of the CNT/GO electrodes, a fact that can be attributed to much higher noise (which is in agreement with what was observed in the differential pulse voltammetry measurements). However, the LoD for the CNT/GO/FeONP electrodes is 7.0 ± 0.7, which is approximately half that of the CNT/GO electrodes, a significant improvement. In a previous publication (Ferrier et al., 2021) we showed that the LoD for a sensor consisting of the type of enzyme film described here on a bare carbon SPE was 67 ± 7 ng/ml. Therefore, it can be seen that these metal oxide decorated carbon nanocomposite electrodes offer significant improvements in sensitivity for propofol detection, with composites of carbon nanotubes and iron oxide nanoparticle decorated graphene oxide offering the greatest improvement. Examples of the raw amperometry data and the sensitivity and limits of detection for the various electrodes, without smoothing and baseline correction, are shown in the Supplementary Information, Fig. S4 and Table S1 respectively.

The LoD of 7.0 ± 0.7 ng/ml compares very favourably with alternative reported propofol detection techniques. It is two orders of magnitude below that of optical techniques such as the fluorescence spectrometry-based approach reported by Diao et al. (2019) (which is reported to achieve a detection limit of 500 ng/ml in buffer solution)
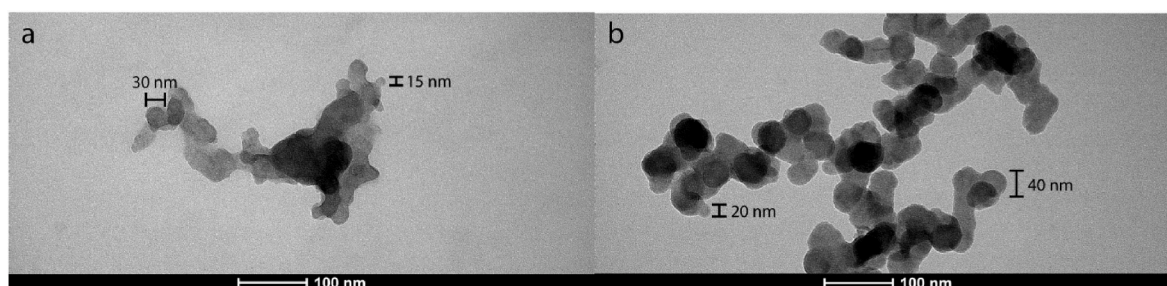
Fig. 2. Transmission electron micrographs of a) iron oxide nanoparticles, b) copper oxide nanoparticles.
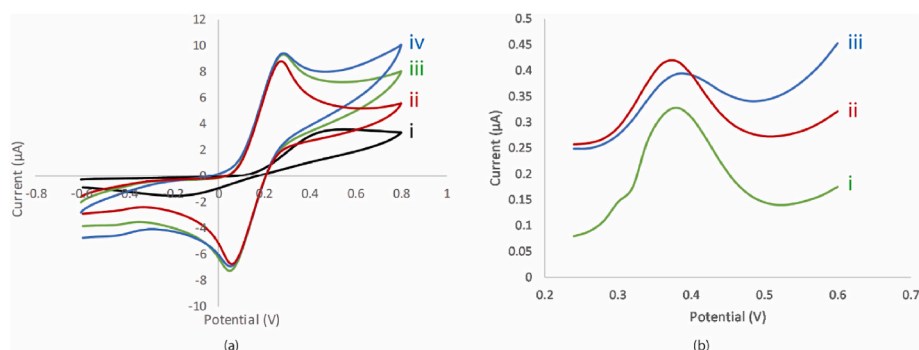
Fig. 3. a) Cyclic voltammograms in 10 mM ferricyanide solution for blank electrode (i), CNT/GO/FeONP functionalised electrode (ii), CNT/GO functionalised electrode (iii), and CNT/GO/CuONP functionalised electrode (iv). Scan rate is 100 mV/s, all potentials are vs. Ag/AgCl. b) Differential pulse voltammograms in 10 µg/ml propofol solution (50 µg/ml NADP$^+$/G6P, 10 mM PBS) for CNT/GO electrode (i), CNT/GO/FeONP electrode (ii), and CNT/GO/CuONP electrode (iii).
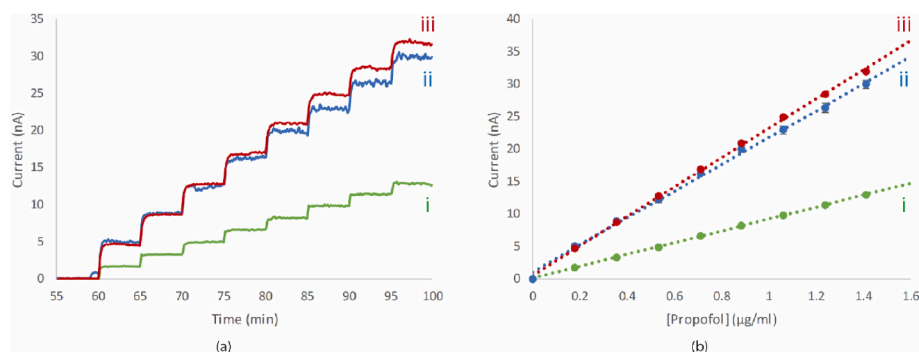
Fig. 4. a) Amperometric response to increasing propofol concentration for sensors functionalised with i) CNT/GO, ii) CNT/GO/CuONP, and iii) CNT/GO/FeONP. Aliquots of propofol stock (20 µl at 1 mM) are injected at 5-min intervals. b) Mean of plateau current against propofol concentration. Solution is 50 µg/ml NADP$^+$/G6P, 10 mM PBS. Error bars represent three standard deviations.

Table 1

Sensitivities and limits of detection for electrodes functionalised with various different nanomaterials. The uncertainties represent the standard error on the mean. Solution is 50 µg/ml NADP$^+$/G6P, 10 mM PBS. N = 3.

Electrode functionalisation	Sensitivity (nA/µg/ml/mm^2)	LoD (ng/ml)
CNT/GO	12.2 ± 0.5	14.2 ± 0.5
CNT/GO/CuONP	18.6 ± 3.8	19.9 ± 3.8
CNT/GO/FeONP	29.9 ± 6.4	7.0 ± 0.7

and the spectrophotometric approach reported by Liu et al. (2012) (detection limit, 270 ng/ml in whole blood), neither of which have been demonstrated for continuous, real-time propofol detection. It is also significantly lower than that of the chemiresistive molecularly imprinted polymer (MIP) sensor reported by Hong et al. (2016), which has a reported detection limit of 100 ng/ml in plasma, and which has also not been demonstrated for continuous monitoring. Of the methods that have been reported for continuous monitoring, the approach described herein compares favourably with the voltametric approaches developed by Carrara et al. One approach reported by this group achieves a detection limit of 146 ng/ml in serum and overcomes electrode fouling by implementing periodic electrode cleaning steps (Stradolini et al., 2018), however, it is unclear how practical this would prove for real-world applications. Another approach reported by this group uses a support vector classifier to compensate for the effects of fouling (Aiassa et al., 2021). They report a detection limit of 428 ng/ml in buffer but have, to date, only demonstrated this approach up to a measurement time of 10 min. The detection limit of our approach also compares favourably with the amperometric approach based on polyvinyl chloride (PVC) membrane coated electrodes developed by Kivlehan et al. (2015), which is reported to achieve a limit of detection of 14.3 ng/ml in buffer solution.

A summary of reported propofol detection techniques and their respective detection limits is presented in Table 2.

To the authors' best knowledge, there have been no other reports of the application of metal oxide nanoparticles or carbon nanocomposites to the detection of propofol. However, there are examples of their application to the detection of similar phenolic molecules. Erogul et al. (2015) have reported sensors based on iron oxide/graphene/gold nanoparticle composites for the detection of hydroquinone and catechol with detection limits of approximately 120 and 90 ng/ml respectively. Pino et al. (2016) have reported a copper oxide nanoparticle-based sensor for the detection of phenol and catechol with detection limits of approximately 65 and 35 ng/ml respectively. Both examples have been developed for the detection of analytes in water samples. The

Table 2

Summary of reported limits of detection for various propofol detection and quantification techniques.

Approach	Limit of detection (ng/ml)	Medium	Reference
Fluorescence spectroscopy	500	Buffer	Diao et al. (2019)
Spectrophotometry	270	Blood	Liu et al. (2012)
Chemiresistive MIP	100	Plasma	Hong et al. (2016)
Voltammetry/pencil graphite	146[a]	Serum	Stradolini et al. (2018)
Voltammetry/support vector classifier	428[a]	Buffer	Aiassa et al. (2021)
Amperometry/PVC membrane	14.3[a]	Buffer	Kivlehan et al. (2015)
CYP450 2B6/nanocomposite	7.0	Buffer	This study

[a] Converted from µM.

performance of the sensor reported herein compares favourably with these examples. Neither group appear to have reported amperometry measurements beyond 15 min in duration, so they have not had to address the electrode fouling issues that are likely when detecting phenolic analytes.

In order to assess the performance of the sensors in conditions more akin to the physiological, amperometry measurements were performed for CNT/GO/FeONP functionalised electrodes in solutions containing 50 µg/ml NADP$^+$ and G6P, 5 wt% BSA and 10 mM PBS (137 mM NaCl, 2.7 mM KCl, pH 7.4). Such solutions are considered 'serum-like' as they possess physiological salinity (Opoku-Okrah et al., 2015), pH (Brørs and Jacobsen, 1985) and albumin concentration (Hill, 1985; Kim et al., 2020). From Fig. 5 it can be seen that the sensor produces a clear response to increasing propofol concentration and produces a linear response across the therapeutic range (1–10 µg/ml (Regenthal et al., 1999)). The sensitivity is significantly reduced compared to the case in buffer solution and the limit of detection (143 ± 27 ng/ml) is significantly higher, but this is as would be expected given that it is known that a large proportion of the propofol will be bound to the albumin and only a minority will exist free in solution (Mazoit and Samii, 1999), and the limit of detection remains an order of magnitude below the lower end of the therapeutic range.

The LoD varies with the quantity of nanomaterial deposited on the working electrode surface (Supplementary Information, Fig. S5). Increasing the quantity of nanomaterial increases the sensitivity of the propofol sensor in a roughly linear manner. However, this also causes the noise to increase approximately exponentially. As a result, the optimal limit of detection is achieved with two sequential depositions of 0.75 µl of the nanomaterial solution, which is the method used for all other electrodes discussed in this paper.

The results of amperometric measurements for a CNT/GO/FeONP electrode with successive additions of 10 µM midazolam, 100 µM cisatricurium besilate and 10 µM fentanyl are shown in Fig. 6. It can be seen that these potential interfering substances produce no change in the current that can be discerned above any noise. Midazolam is a sedative that is commonly administered prior to the application of general anaesthesia (Wong et al., 1991), cisatracurium besilate is a neuromuscular blocker (muscle relaxant) that is widely used in surgery and commonly co-administered with propofol (Guo et al., 2017; Ayad et al., 2018), and fentanyl is a synthetic opioid commonly used as a perioperative drug (Peng and Sandler, 1999). Midazolam and fentanyl are injected at a concentration of 10 µM as their therapeutic ranges are approximately two orders of magnitude below that of propofol (0.04–0.1 and 0.005–0.3 µg/ml respectively) and cisatricurium besilate is injected at a concentration of 100 µM as its therapeutic range is approximately one order of magnitude lower than that of propofol (≤1.3 µg/ml) (Regenthal et al., 1999).

Similar experiments using lidocaine (1 mM) and morphine (10 µM)
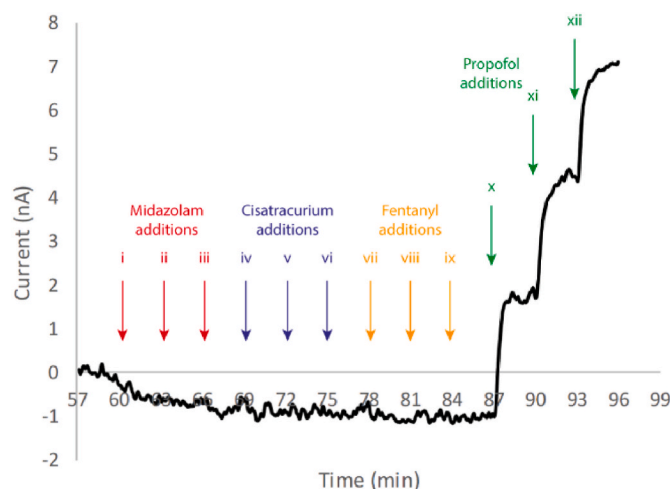
Fig. 6. Amperometric response of CNT/GO/FeO NP/enzyme functionalised electrode with successive injections of Midazolam solution (i-iii; 0.0033, 0.0065 and 0.0097 µg/ml respectively), cisatracurium besilate solution (iv-vi; 0.12, 0.25 and 0.37 µg/ml respectively), fentanyl solution (vii-ix; 0.0018, 0.0035 and 0.0053 µg/ml respectively) and propofol solution (x-xii; 0.18, 0.35 and 0.53 µg/ml respectively). Potential is +0.5 V vs. screen-printed Ag/AgCl. Solution is 10 mM PBS containing 50 µg/ml NADP$^+$ and 50 µg/ml G6P.

also show no discernible response from the sensor (Supplementary Information, Fig. S6). Lidocaine is significant as it is a local anaesthetic that is often administered prior to or during general anaesthesia (Bahk and Lim, 2001; Altermatt et al., 2012) and is also metabolised by the enzyme cytochrome P450 2B6 (Imaoka et al., 1996), whereas morphine is one of the most commonly used opiates and is frequently administered during surgical procedures (Abraham et al., 2020). Lidocaine is injected at the same concentration as propofol (1 mM) as its therapeutic range (1–6 µg/ml) is of the same order of magnitude as that of propofol (1–10 µg/ml), whereas morphine is injected at 10 µM as its therapeutic range (0.01–0.15 µg/ml) is two orders of magnitude below that of propofol (Regenthal et al., 1999).

In order to assess the shelf-life of these sensors, CNT/GO/FeONP electrodes were prepared and amperometry measurements performed as described previously at various intervals after their fabrication. The current response to increasing propofol concentration remains relatively consistent across a seven-day period (having a coefficient of variation of 0.04), with any variation in sensitivity accountable for by interelectrode variation (Supplementary Information, Fig. S6). Therefore, it appears that these sensors remain stable for at least a week when stored at 4 °C.
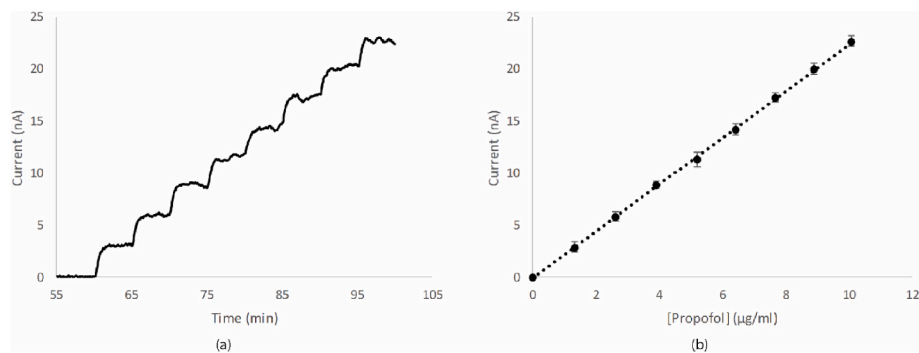
Fig. 5. a) Amperometric response of CNT/GO/FeONP electrode at +500 mV to increasing propofol concentration. Aliquots of propofol stock (150 µl at 1 mM) are injected at 5-min intervals. b) Mean of plateau current against propofol concentration. Solution is 50 µg/ml NADP$^+$/G6P, 5 wt% BSA, 10 mM PBS. Error bars represent three standard deviations.

4. Concluding remarks

We have demonstrated a cytochrome P450 2B6/carbon/metal oxide nanocomposite sensor for continuous propofol monitoring. We compared three different nanocomposites and found that carbon nanotube/iron oxide nanoparticle-decorated graphene oxide produced the most favourable results. This nanocomposite is synthesised using a simple 'green synthesis' approach. To the authors' best knowledge, this represents one of very few applications of the green synthesis of nanoparticles to sensor development.

The sensor has a limit of detection of 7.0 ± 0.7 ng/ml which represents an order of magnitude improvement over an equivalent sensor consisting of just the enzyme immobilised on a bare graphite electrode. The sensor displays a sensitivity of 29.9 ± 6.4 nA/µg/ml/mm^2 and a linear response across the therapeutic range of propofol in a 'serum-like' solution. The sensor has been shown to have good selectivity towards several common perioperative drugs and shows no sign of electrode passivation.

Future work will include incorporating this sensor into a microdialysis device (Baldini, 2010) so as to enable the continuous monitoring of propofol in a patient's bloodstream without requiring the drawing of blood. This approach has several advantages including the avoidance of any potential protein fouling and allowing a degree of control over the composition of the sensing medium, such as the incorporation of NADP$^+$.

CRediT authorship contribution statement

David C. Ferrier: Conceptualization, Methodology, Investigation, Writing – original draft, Writing – review & editing. **Janice Kiely:** Writing – review & editing, Funding acquisition. **Richard Luxton:** Writing – review & editing, Funding acquisition.

Declaration of competing interest

The authors declare the following financial interests/personal relationships which may be considered as potential competing interests: David Ferrier reports writing assistance was provided by Somnus Scientific Ltd. David Ferrier, Janice Kiely, Richard Luxton have patent #GB2596513 pending to Somnus Scientific Ltd.

Data availability

Data will be made available on request.

Appendix A. Supplementary data

Supplementary data to this article can be found online at https://doi.org/10.1016/j.biosx.2022.100286.

References

Abraham, P., Renjini, S., Vijayan, P., Nisha, V., Sreevalsan, K., Anithakumaray, V., 2020. J. Electrochem. Soc. 167, 037559.
Aiassa, S., Hanitra, I.N., Sandri, G., Totu, T., Grassi, F., Criscuolo, F., De Micheli, G., Carrara, S., Demarchi, D., 2021. Biosens. Bioelectron. 171, 112666.
Alagiri, M., Hamid, S.B.A., 2014. J. Mater. Sci. Mater. Electron. 25, 3572–3577.
Altermatt, F.R., Bugedo, D.A., Delfino, A.E., Solari, S., Guerra, I., Muñoz, H.R., Cortínez, L.I., 2012. Br. J. Anaesth. 108, 979–983.
Aryal, K.P., Jeong, H.K., 2019. Chem. Phys. Lett. 723, 133–138.
Asadian, E., Shahrokhian, S., Zad, A.I., Ghorbani-Bidkorbeh, F., 2017. Sensor. Actuator. B Chem. 239, 617–627.
Ayad, M.M., Belal, F., Hosney, M.M., Elmansi, H., Elsayed, N., 2018. J. Chromatogr. Sci. 56, 524–530.
Bagbi, Y., Sarswat, A., Mohan, D., Pandey, A., Solanki, P.R., 2017. Sci. Rep. 7, 7672.
Bahk, J.-H., Lim, Y.-J., 2001. Anesth. Analg. 92, 1073–1077.
Baldini, F., 2010. Anal. Bioanal. Chem. 397, 909–916.
Barr, J., Egan, T.D., Sandoval, N.F., Zomorodi, K., Cohane, C., Gambus, P.L., Shafer, S.L., 2001. Anesthesiol 95, 324–333.
Barr, J., Fraser, G.L., Puntillo, K., Ely, E.W., Gélinas, C., Dasta, J.F., Davidson, J.E., Devlin, J.W., Kress, J.P., Joffe, A.M., Coursin, D.B., Herr, D.L., Tung, A., Robinson, B.R.H., Fontaine, D.K., Ramsay, M.A., Riker, R.R., Sessler, C.N., Pun, B., Skrobik, Y., Jaeschke, R., 2013. Crit. Care Med. 41, 263–306.
Brørs, O., Jacobsen, S., 1985. Br. J. Clin. Pharmacol. 20, 85–88.
Campbell, M., Pierce, J.M.T., 2015. BJA Educ 15, 173–179.
Cesar, I., Sivula, K., Kay, A., Zboril, R., Grätzel, M., 2009. J. Phys. Chem. B 113, 772–782.
Chen, M., Hou, C., Huo, D., Yang, M., Fa, H., 2016. Appl. Surf. Sci. 364, 703–709.
Diao, J., Wang, T., Li, L., 2019. R. Soc. Open Sci. 6, 181753.
El Ghandoor, H., Zidan, H.M., Khalil, M.M.H., Ismail, M.I.M., 2012. Int. J. Electrochem. Sci. 7, 5734–5745.
Erogul, S., Bas, S.Z., Ozmen, M., Yildiz, S., 2015. Electrochim. Acta 186, 302–313.
Fakhari, S., Jamzad, M., Fard, H.K., 2019. Green Chem. Lett. Rev. 12, 19–24.
Ferreira, M., Varela, H., Torresi, R.M., Tremiliosi-Filho, G., 2006. Electrochim. Acta 52, 434–442.
Ferrier, D.C., Kiely, J., Luxton, R., 2021. IEEE Sensor. J. 21, 23730–23736.
Ferrier, D.C., Kiely, J., Luxton, R., 2022. J. Clin. Monit. Comput. 36, 315–323.
Ghidan, A.Y., Al-Antary, T.M., Awwad, A.M., 2016. Environ. Nanotechnol. Monit. Manag. 6, 95–98.
Gilbert, B., Frandsen, C., Maxey, E.R., Sherman, D.M., 2009. Phys. Rev. B 79, 035108.
Guo, J., Yuan, X., Zhou, X., Jin, X., 2017. J. Clin. Anesth. 38, 75–80.
Hill, P.G., 1985. Ann. Clin. Biochem. 22, 565–578.
Hong, C.-C., Lin, C.-C., Hong, C.-L., Lin, Z.-X., Chung, M.-H., Hsieh, P.-W., 2016. Biosens. Bioelectron. 86, 623–629.
Hwa, K.-Y., Subramani, B., 2014. Biosens. Bioelectron. 62, 127–133.
Imaoka, S., Yamanda, T., Hiroi, T., Hayashi, K., Sakaki, T., Yabusaki, Y., Funae, Y., 1996. Biochem. Pharmacol. 51, 1041–1050.
Jamzad, M., Bidkorpeh, M.K., 2020. J. Nanostruct. Chem. 10, 193–201.
Kamali, K.Z., Alagarsamy, P., Huang, N.M., Ong, B.H., Lim, H.N., 2014. Sci. World J. 2014, 396135.
Kim, J.W., Byun, M.S., Lee, J.H., Yi, D., Jeon, S.Y., Sohn, B.K., Lee, J.-Y., Shin, S.A., Kim, Y.K., Kang, K.M., Sohn, C.-H., Lee, D.Y., 2020. Neurol. 95, e815–e826.
Kivlehan, F., Chaum, E., Lindner, E., 2015. Analyst 140, 98–106.
Kobylinska, N., Klymchuk, D., Shakhovsky, A., Khainakova, O., Ratushnyak, Y., Duplij, V., Matvieieva, N., 2021. RSC Adv. 11, 26974–26987.
Kumar, J.N., Reddy, V.A., Marjorie, S.R., Thanikaikarasan, S., 2020. Mater. Today Proc. 33, 2961–2963.
Lassoued, A., Lassoued, M.S., Dkhil, B., Ammar, S., Gadri, A., 2018. Phys. E Low-dimens. Syst. Nanostruct. 97, 328–334.
Laurila, T., Sorajärvi, T., Saarela, J., Toivonen, J., Wheeler, D.W., Ciaffoni, L., Ritchie, G.A.D., Kaminski, C.F., 2011. Anal. Chem. 83, 3963–3967.
Lewis, M.C., Nevo, I., Paniagua, M.A., Ben-Ari, A., Pretto, E., Eisdorfer, S., Davidson, E., Matot, I., Eisdorfer, C., 2007. Med. Hypotheses 68, 484–492.
Lim, W.Q., Gao, Z., 2015. Electroanalysis 27, 2074–2090.
Liu, B., Pettigrew, D.M., Bates, S., Laitenberger, P.G., Troughton, G., 2012. J. Clin. Monit. Comput. 26, 29–36.
Madhurantakam, S., Babu, K.J., Rayappan, J.B.B., Krishnan, U.M., 2017. Biosens. Bioelectron. 87, 832–841.
Makarov, V.V., Love, A.J., Sinitsyna, O.V., Makarova, S.S., Yaminsky, I.V., Taliansky, M.E., Kalinina, N.O., 2014. Acta Nat. 6, 35–44.
Mazoit, J.X., Samii, K., 1999. Br. J. Clin. Pharmacol. 47, 35–42.
Mdletshe, L.S., Makgwane, P.R., Ray, S.S., 2019. Nanomaterials 9, 1140.
Mellon, R.D., Simone, A.F., Rappaport, B.A., 2007. Pediatric Anesth 104, 509–520.
Opoku-Okrah, C., Acquah, B.K.S., Dogbe, E.E., 2015. Pan Afr. Med. J. 20, 236.
Peng, P.H.W., Sandler, A.N., 1999. Anesthesiology (Hagerst.) 90, 576–599.
Pino, F., Mayorga-Martinez, C.C., Merkoçi, A., 2016. Electrochem. Comm. 71, 33–37.
Radoń, A., Drygała, A., Hawelek, Ł., Łukowiec, D., 2017. Mater. Char. 131, 148–156.
Regenthal, R., Krueger, M., Koeppel, C., Preiss, R., 1999. J. Clin. Monit. 15, 529–544.
Rostamabadi, P.F., Heydari-Bafrooei, E., 2019. Microchim. Acta 186, 495.
Ryan, S.M., Nielsen, C.J., 2010. Anesth. Analg. 111, 92–98.
Sahinovic, M.M., Struys, M.M.R.F., Absalom, A.R., 2018. Clin. Pharmacokinet. 57, 1539–1558.
Shi, J.-B., Lee, C.-W., Guo, J.-W., Cheng, M.-J., Wu, C., Chen, C.-J., Chen, Y.-C., Lin, Y.-T., Chang, C.-C., 2007. Mater. Lett. 61, 5268–5270.
Srivastava, S., Kumar, M., Agrawal, A., Dwivedi, S.K., 2013. IOSR J. Appl. Phys. 5, 61–65.
Tak, M., Gupta, V., Tomar, M., J. Mater. Chem. B, 1, 6392-6401.
Stradolini, F., Kilic, T., Taurino, I., De Micheli, G., Carrara, S., 2018. Sensor. Actuator. B Chem. 269, 304–313.
Thielsch, R., Böhme, T., Reiche, R., Schläfer, D., Bauer, H.-D., Böttcher, H., 1998. Nanostruct. Mater. 10, 131–149.

Tung, T.T., Chien, N.V., Duy, N.V., Hieu, N.V., Nine, M.J., Coghlan, C.J., Tran, D.N.H., Losic, D., 2019. J. Colloid Interface Sci. 539, 315–325.

Viezbicke, B.D., Patel, S., Davis, B.E., Birnie, D.P., 2015. Phys. Status Solidi B 252, 1700–1710.

Vollmer, M.K., Rhee, T.S., Rigby, M., Hostetter, D., Hill, M., Schoenenberger, F., Reimann, S., 2015. Geophys. Res. Lett. 42, 1606–1611.

Wall, T., Sherwin, A., Ma, D., Buggy, D.J., 2019. Br. J. Anaesth. 123, 135–150.

Wayu, M.B., Spidle, R.T., Devkota, T., Deb, A.K., Delong, R.K., Ghosh, K.C., Wanekaya, A. K., Chusuei, C.C., 2013. Electrochim. Acta 97, 99–104.

Wigmore, T.J., Mohammed, K., Jhanji, S., 2016. Anesthesiol 124, 69–79.

Wong, H.Y., Fragen, R.J., Dunn, K., 1991. Anesthesiol 74, 675–679.

Xie, Z., Dong, Y., Maeda, U., Moir, R.D., Xia, W., Culley, D.J., Crosby, G., Tanzi, R.E., 2007. J. Neurosci. 27, 1247–1254.

Yamamoto, K., 2020. Anaesthesiol. Intensive Ther. 52, 354–355.

Yang, X., Kirsch, J., Fergus, J., Simonian, A., 2013. Electrochim. Acta 94, 259–268.

Zhang, F., Dong, H., Zhang, X., Guo, J., Liu, Y., Zhou, C., Zhang, X., Liu, J., Yan, M., Chen, X., 2017. Anal. Sci. 33, 1271–1277.

Zhao, P., Chen, C., Ni, M., Peng, L., Li, C., Xie, Y., Fei, J., 2019. Microchim. Acta 186, 134.

Zikalala, N., Matshetshe, K., Parani, S., Oluwafemi, O.S., 2018. Nano-Struct. Nano-Objects 16, 288–299.